Interplay of spin current and magnetization in a topological-insulator/magnetic-insulator bilayer structure

Xiaohang Zhang [1,2] Connie H. Li,[2] Jisoo Moon,[2] Serhiy Leontsev [3] Michael R. Page,[3]
Berend T. Jonker,[2] and Olaf van 't Erve[2,*]
[1]NOVA Research, Inc., 1900 Elkin St. #230, Alexandria, Virginia 22308, USA
[2]Magnetoelectronic Materials & Devices, Materials Science & Technology Division, Naval Research Laboratory, 4555 Overlook Ave. SW, Washington D.C. 20375, USA
[3]Materials and Manufacturing Directorate, Air Force Research Laboratory, Wright-Patterson Air Force Base (WPAFB), Ohio 45433, USA

(Received 1 November 2021; revised 9 May 2022; accepted 29 June 2022; published 20 July 2022)

The interaction between accumulated spins on the surface of a heavy metal (HM) and the magnetization of an adjacent magnetic material leads to various spin phenomena, such as spin-orbit torque, spin pumping, and spin Hall magnetoresistance (SHMR). However, the exploration of device applications based on these spin phenomena is often limited by the low charge-to-spin conversion efficiency of the HM. Authors of recent studies have suggested that topological insulators (TIs) are promising candidates for device applications due to their potentially higher charge-to-spin conversion efficiency. Here, we report a multifaceted study of a bilayer structure consisting of Bi_2Se_3 and Y_3Fe_5O (YIG) and demonstrate an approach based on angle-dependent magnetoresistance (ADMR) measurements to determine the effective charge-to-spin conversion efficiency in TIs. Our ferromagnetic resonance measurements demonstrate efficient spin pumping from YIG to Bi_2Se_3, which is further confirmed by detection of an electromotive force generated in Bi_2Se_3 via spin-to-charge conversion. Our ADMR measurements show that the interfacial spin diffusion can significantly affect the charge transport in a way like the SHMR effect and provide an estimate of the charge-to-spin conversion efficiency in Bi_2Se_3 of ~0.1–0.4. Neglecting to account for the large out-of-plane magnetoresistance of the Bi_2Se_3 results in a fivefold overestimate of the charge-to-spin conversion efficiency.

DOI: 10.1103/PhysRevMaterials.6.074203

I. INTRODUCTION

Joule heating, parasitic conduction, and magnetic fringe fields severely constrain the operation and scaling of spintronic devices [1]. To reduce these undesirable issues, a great deal of attention has focused on the generation, detection, and use of pure spin current to alter the magnetization of layers within the device structure. However, a pure spin current can be generated only by a few methods, including spin pumping [2,3], spin Hall effect (SHE) [4], and spin Seebeck effect (SSE) [5].

The SHE exploits the strong spin-orbit coupling (SOC) of heavy metals (HMs): when a charge current passes through a HM, the SHE causes electrons with opposite spins to scatter in opposite directions and thus generates a transverse spin current/accumulation with a density proportional to the spin Hall angle θ_{SH}. In a case where the HM is in close proximity to a ferromagnet (FM), the interaction between the accumulated spins and the magnetization of the FM at the interface results in spin-orbit torque (SOT) in the FM and thus provides an effective way to manipulate the magnetization of the FM at the nanoscale [6]. Specifically, using this current-induced SOT for memory applications in a SOT magnetoresistive random-access memory (MRAM) can significantly reduce the energy consumption as compared with using a spin-polarized charge current for magnetization switching in a conventional spin-transfer torque MRAM [7].

In addition, reflection of the transverse spin current back into the HM from the interface induces an extra conduction term via the inverse SHE (ISHE) and thus reduces the electrical resistance of the bilayer structure. However, this reflection process can be suppressed when the accumulated spins at the surface of the HM are not collinear with the magnetization of the FM, as a part of transverse spin current is absorbed by the magnetization of the FM through the interfacial SOT effect [8]. Therefore, the longitudinal resistance of the HM-FM structure varies as the direction of the magnetization changes, which is known as the spin Hall magnetoresistance (SHMR) and characterized by $R^y < R^z \approx R^x$, where R^i is the resistance measured when the magnetization is saturated along $i = x$ (current direction), y (in-plane and perpendicular to the current), and z (normal to the interface) [9]. Moreover, since the SHMR arises directly from the charge-spin interconversion in the bilayer structure, the SHMR ratio is expected to qualitatively reflect the magnitude of the spin Hall angle [10].

The charge-to-spin conversion efficiency in HM-FM structures has been limited by the relatively small spin Hall angle of conventional HMs (e.g., Pt, W, and Ta) and/or high damping at the interface. Recently, it was suggested that topological insulators (TIs) could exhibit a much higher charge-to-spin

*olaf.vanterve@nrl.navy.mil

TABLE I. Estimated values of the effective spin Hall angle for various TIs.

TI	Sample structure	Temperature	Experimental method	Effective spin Hall angle ($\theta_{\mathrm{eff\,SH}}$)	Reference
Bi_2Se_3	Bi_2Se_3/Py	300 K	ST-FMR	2.0–3.5	[11]
Bi_2Se_3	Bi_2Se_3/Fe	20 K	ST-FMR	0.8–4.9	[21]
Bi_2Se_3	Bi_2Se_3/Fe	300 K	ST-FMR	0.2–0.7	[21]
Bi_2Se_3	Bi_2Se_3/CoFeB	3 K	ST-FMR	1.62–2.1	[22]
$(Bi_{1-x}Sb_x)_2Te_3$	$(Bi_{1-y}Sb_y)_2Te_3$/Cu/Py	10 K	ST-FMR	0.45–0.57	[23]
Bi_2Se_3	Bi_2Se_3/Py	300 K	ST-FMR and IREE	0.0093	[18]
Bi_2Se_3	Bi_2Se_3/CoFeB	300 K	ST-FMR and IREE	0.021–0.43	[19]
Bi_2Se_3	Bi_2Se_3/YIG	300 K	ST-FMR and IREE	0.022	[20]
Bi_2Se_3	Bi_2Se_3/MgO/CoFeB	4 K	IREE	0.8	[12]
Bi_2Se_3	Bi_2Se_3/Py	300 K	IREE	0.4	[17]
$(Bi_{0.5}Sb_{0.5})_2Te_3$	$(Bi_{0.5}Sb_{0.5})_2Te_3/(Cr_{0.08}Bi_{0.54}Sb_{0.38})_2Te_3$	1.9 K	Second harmonic AHE	140–425	[15]
$(Bi_{1-y}Sb_y)_2Te_3$	$(Bi_{1-y}Sb_y)_2Te_3/Cr_x(Bi_{1-y}Sb_y)_{2-x}Te_3$	2 K	Second harmonic AHE	160	[16]
Bi_2Se_3	Bi_2Se_3/YIG	20 K	ST-FMR, IREE, and ADMR	0.1–0.4	This paper

conversion efficiency, which is often represented by a large effective spin Hall angle (θ_{effSH}) [11–13]. Specifically, in a TI, a charge current flowing through the surface induces spontaneous spin accumulation due to spin-momentum locking (SML) of the surface states. This current-induced surface spin accumulation is often considered a quantum limit of the SHE [12,14], and the charge-to-spin conversion efficiency is expected to be large. Experimentally, the effective spin Hall angle of TIs reported in previous studies [11,12,15–23] ranges from $\sim$0.01 to >400 (Table I), demonstrating a large discrepancy in the measured charge-to-spin conversion efficiency of the TIs.

On the other hand, recent angle-dependent magnetoresistance (ADMR) measurements performed on several TI-FM structures reported a magnetoresistance (MR) ratio of $\sim$0.3–1.0% [24–27], which is much larger than the SHMR ratio of HM-FM structures and consistent with the expected large charge-to-spin conversion efficiency. However, it is interesting to note that the resistance measured on these TI-FM structures does not show the characteristic relationship expected for the SHMR of HM-FM structures, i.e., $R^y < R^z \approx R^x$, or for the anisotropic MR (AMR) of a FM, i.e., $R^y \approx R^z < R^x$ [28]. Therefore, to fully understand the transport mechanism in TI-FM structures, further investigation is required as reported here.

Another important aspect of the interplay of spin current and magnetization in a TI-FM structure is spin pumping, where a spin current/accumulation generated in the FM by FM resonance (FMR) diffuses into the TI [29]. The spin pumping and accompanying spin backflow lead to broadened FMR linewidths and an enhanced Gilbert damping constant for magnetization precession [30]. Further, analogous to the spin-to-charge conversion (SCC) in HMs via the ISHE, the pure spin current generated by spin pumping induces a charge electromotive force (emf) in the TI via the inverse Rashba-Edelstein effect (IREE), providing a way to electrically detect the spin-pumping effect and the SCC. To date, in most electrical measurements of the emf induced in TIs, the spin current was generated by spin pumping from a FM metal [18,19,31,32]. The small effective spin Hall angle of TIs reported in these studies has been attributed to electron diffusion at the interface, which leads to degradation of the helical Dirac states [33] and to current shunting through the FM metal, which reduces the emf signal.

In this paper, we provide a comprehensive study of the interplay of spin current and magnetization in a bilayer structure consisting of Bi_2Se_3 and Y_3Fe_5O (YIG). The insulating nature of the ferrimagnetic insulator YIG eliminates current shunting and the dissipation caused by the conduction electrons in the FM and thus provides a more accurate measurement of the charge-to-spin interconversion efficiency in Bi_2Se_3 [34,35]. Our FMR measurements exhibit broadening of the FMR linewidth because of spin pumping from YIG to Bi_2Se_3, with an extracted effective spin-mixing conductance (G_{eff}) of $5.0 \times 10^{13}\ \Omega^{-1}\,\mathrm{m}^{-2}$. At the FMR frequency, a static voltage is observed in Bi_2Se_3 in a direction perpendicular to the applied magnetic field, providing evidence for the conversion of spin current into emf in the TI. We further carried out ADMR measurements of the Bi_2Se_3-YIG bilayer structure and observed a moderate variation when the external magnetic field rotates within the sample plane but a pronounced enhancement when the field rotates away from the sample plane. By comparing the ADMR result with that of a reference Bi_2Se_3 thin film, we found that the intrinsic ADMR of the TI must be considered, and the MR ratio associated with the interfacial interaction between YIG and Bi_2Se_3 is $\sim$0.04% at 20 K. Based on the effective spin-mixing conductance and the MR ratio obtained in our measurements, we further demonstrated an approach to determine the SCC efficiency in the TI and estimated that the effective spin Hall angle of Bi_2Se_3 is in a range of $\sim$0.1–0.4.

II. SAMPLE PREPARATION AND MEASUREMENTS

The samples studied in this paper include two Bi_2Se_3(20 nm)-YIG(10 nm) bilayer samples, a YIG (10 nm) reference sample, and a Bi_2Se_3 (20 nm) reference sample. The high-quality ultrathin YIG films were epitaxially grown on $10 \times 10\,\mathrm{mm}^2$ single-crystal Gd_3Ga_5O (111) substrates (MTI Corp) in a custom-made high-vacuum pulse laser deposition (PLD) system. Cleaned substrates were introduced into the growth chamber via load lock (base pressure $<10^{-8}$ Torr) and heated to 825 °C. Deposition was carried out by ablating a ceramic YIG target with a KrF excimer laser (Lambda Physik LPX 305i, $\lambda = 248$ nm) under an oxygen pressure of

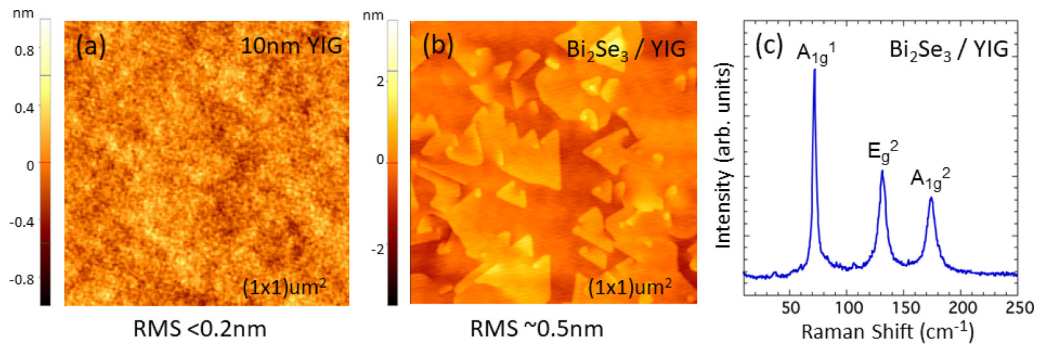

FIG. 1. (a) Atomic force microscopy (AFM) image of a 10 nm YIG film grown on a Gd_3Ga_5O (111) substrate. (b) AFM image of a 20 nm Bi_2Se_3 film grown on 10 nm of YIG. (c) Raman spectrum of a Bi_2Se_3-YIG structure.

100 mTorr followed by cooling down to room temperature without annealing. PLD growth parameters were optimized to obtain the desired thickness (10 nm) while maintaining low microwave losses of the YIG layers (confirmed by x-ray reflectivity and FMR measurements, respectively) [36]. Bi_2Se_3 films were subsequently grown on air-exposed YIG films by molecular beam epitaxy (MBE) using a two-step method [37]. The Bi_2Se_3 reference sample was grown on a sapphire substrate using the same method.

A commercial CryoFMR from NanoOsc combined with a Montana magneto-optic cryostat was used for all FMR measurements. This system uses a coplanar waveguide and a small AC modulation magnetic field to detect the rectified transmitted RF signal by lock-in techniques. The RF range is 2–18 GHz, while the temperature range is 4–350 K.

For MR measurements, the Bi_2Se_3-YIG and Bi_2Se_3 reference samples are patterned into Hall bars with a channel width of 500 μm and a channel length of 2 mm. MR results are obtained in a Janis CCS-350 cryostat equipped with a rotatable magnet capable of supplying a 1 Tesla field.

III. RESULTS AND DISCUSSIONS

Bi_2Se_3, the prototypical three-dimensional (3D) TI, is a layered material, where five atomic planes of Se-Bi-Se-Bi-Se form a quintuple layer unit. Its anisotropic strong covalent intralayer bonding and weak van der Waals (vdW) interlayer bonding facilitate its growth on a variety of substrates via vdW epitaxy [37–40]. Figure 1(a) is an atomic force microscopy (AFM) image of a 10 nm YIG film grown on a $Gd_3Ga_5O_{12}$ (111) substrate. The remarkably low root mean square (RMS) roughness of the YIG film (<0.2 nm) and a much lower growth temperature for Bi_2Se_3 than for YIG suggest that a sharp interface can be formed in YIG-TI bilayer structures. Figure 1(b) is an AFM image showing the surface morphology of a 20 nm Bi_2Se_3 film grown on 10 nm YIG. The appearance of triangular islands is characteristic of its hexagonal crystalline symmetry, and the low RMS roughness (∼0.5 nm) indicates the high quality of the MBE-grown Bi_2Se_3. Figure 1(c) shows a typical Raman spectrum of Bi_2Se_3-YIG, which exhibits characteristic peaks at 73, 136, and 176 cm^{-1}, attributed to the A_{1g}^1, E_g^2, and A_{1g}^2 vibrational modes expected for the Bi_2Se_3.

YIG is a magnetic insulator that has been widely used as a source for resonantly exciting spin current. The absence of dissipation caused by conduction electron scattering leads to a small Gilbert damping constant α [41–43]. Figure 2(a) shows representative FMR spectra of a YIG reference sample and a Bi_2Se_3-YIG bilayer sample at 5 K. Plotted here is the derivative of the transmitted RF power of the coplanar waveguide (with sample facing down) as a function of applied in-plane field. A shift in the resonance field and a broadened linewidth are clearly seen for the Bi_2Se_3-YIG bilayer samples, indicating that the presence of the TI layer alters the dynamic magnetic properties of the YIG layer.

For more quantitative analysis, each spectrum is fitted with the derivative of a single Lorentzian function, yielding two characteristic parameters of the FMR resonance: the resonance field H_{res} and the full width at half maximum ΔH. Figure 2(b) illustrates the frequency dependence on the resonance field H_{res} of the YIG reference and the Bi_2Se_3-YIG bilayer samples measured at 5 K, also known as the Kittel plot. We calculate the effective anisotropy field M_{eff} for different temperatures by fitting the data with the Kittel Eq. (1):

$$f = \frac{g\mu_B}{\hbar}\mu_0\sqrt{H_{res}(H_{res} + M_{eff})}, \quad (1)$$

where $\hbar$ is the Planck's constant, g the Landé factor, μ_0 the permeability of free space, μ_B the Bohr magneton, and $\mu_0 M_{eff} = \mu_0 M_S - \mu_0 H_{an}$, which includes the saturation-magnetization (demagnetizing) field $\mu_0 M_S$ and the out-of-plane uniaxial magnetoelastic anisotropy field $\mu_0 H_{an}$. As shown in Fig. 2(c), the effective anisotropy field $\mu_0 M_{eff}$ as a function of temperature increases from 0.25 T at 300 K to 0.3 T at 5 K for Bi_2Se_3-YIG and is larger than the bulk saturation-magnetization field ($\mu_0 M_S \approx 0.18$ T) of YIG over the entire temperature range. This substantial enhancement is indicative of the significant contribution of the topological surface states (TSSs) to the interfacial coupling between the TI and the FM [44]. The result also indicates a negative sign for the out-of-plane uniaxial magnetoelastic anisotropy field $\mu_0 H_{an}$, which is consistent with the in-plane magnetic anisotropy of the YIG film. The third free parameter in the Kittel fit is the gyromagnetic ratio $\gamma = g\mu_B/\hbar$, which is consistently $\sim 1.8 \pm 0.2 \times 10^{11}$/Ts for all fits.

The linewidth broadening of the absorption peak provides a quantitative measure of the additional damping caused by spin pumping from YIG into Bi_2Se_3 in the bilayer structure [45]. As seen in Fig. 2(a), the FMR linewidth is significantly widened by the addition of the Bi_2Se_3 layer. The spin damping

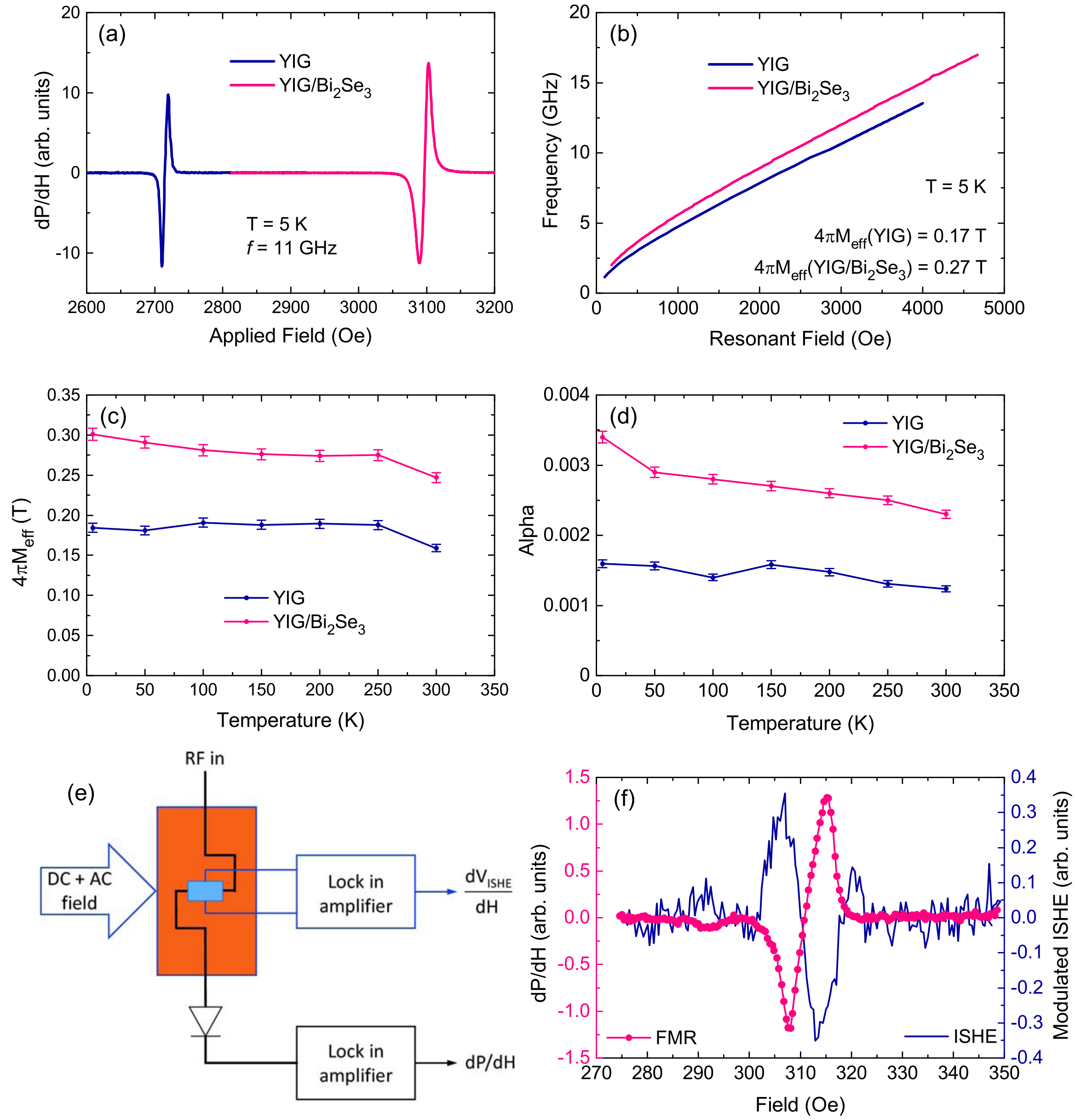

FIG. 2. (a) Ferromagnetic resonance (FMR) response for a YIG film and a YIG-Bi_2Se_3 bilayer at 11 GHz and 5 K. (b) Resonance frequency as a function of magnetic field (Kittel curve) for YIG and YIG-Bi_2Se_3 bilayer. (c) Calculated effective anisotropy field $\mu_0 M_{\rm eff}$ as a function of temperature. (d) Temperature dependence of the Gilbert damping constant (α). (e) Schematic of the inverse Rashba-Edelstein effect (IREE) measurement setup; a pair of small bias coils are used to apply a modulated magnetic field. The rectified RF output of the transmission line and the electromotive force (emf) across the YIG-Bi_2Se_3 sample are measured simultaneously at the modulation frequency. (f) FMR curve (red) and emf (blue) as a function of magnetic field at 3 GHz and 5 K.

effect in FMR is typically described by the Gilbert damping constant α, which can be calculated from the frequency dependence of the linewidth following the linear relation:

$$\Delta H = \Delta H_0 + \frac{2\pi}{\gamma \mu_0}\alpha f, \qquad (2)$$

where ΔH_0 is the extrapolated zero-frequency linewidth (examples of linear fits to experimental data are shown in Fig. S1 in the Supplemental Material [46]). Figure 2(d) shows the temperature dependence of α for the Bi_2Se_3-YIG bilayer and the YIG reference samples. The value of α is nearly constant at 0.0015 for the entire temperature range for the YIG, while it increases from 0.0023 at 300 K to 0.0034 at 5 K for the Bi_2Se_3-YIG bilayer sample. The latter suggests an enhancement of the spin-pumping strength, which is parameterized by an effective spin-mixing conductance $G_{\rm eff}$:

$$\alpha = \alpha_0 + \frac{\gamma \hbar^2}{2e^2 M_S t_{\rm FM}} G_{\rm eff}, \qquad (3)$$

where α and α_0 are the Gilbert damping constants of the Bi_2Se_3-YIG bilayer and the YIG reference sample, respectively, and $t_{\rm FM}$ is the thickness of the YIG layer [47,48]. Calculation based on the equation yields $G_{\rm eff} \approx 5.0 \times 10^{13} \Omega^{-1}\,{\rm m}^{-2}$ for the Bi_2Se_3-YIG interface at 5 K, consistent with earlier results for TI-YIG [14,20] and HM-YIG [49–51] structures.

The effective spin-mixing conductance G_{eff} of an HM-FM interface can be further deconvoluted into two components: the interfacial spin-mixing conductance $G_{\uparrow\downarrow}$, and the bulk spin conductance [inverse of the second term in Eq. (4)] determined by the resistivity ρ, spin diffusion length λ_S, and thickness t_{HM} of the HM layer [21,52,53]:

$$\frac{1}{G_{\mathrm{eff}}} = \frac{1}{G_{\uparrow\downarrow}} + 2\rho\lambda_S \coth\left(\frac{t_{\mathrm{HM}}}{\lambda_S}\right), \tag{4}$$

However, taking the reported spin-diffusion length of 6.2 nm [18] or 1.6 nm [20] for Bi_2Se_3, the thickness and resistivity of the Bi_2Se_3, and G_{eff} calculated above, we obtain a negative $G_{\uparrow\downarrow}$ value, which is certainly unphysical. In fact, such a negative value is typically obtained when directly applying Eq. (4) to a variety of Bi_2Se_3-FM structures [21]. An immediate inspection of the calculation process raises the question about the value used for the relevant resistivity of Bi_2Se_3. By definition, a TI consists of an insulating (gapped) bulk and metallic surface states and thus does not exhibit a uniform/homogeneous electronic structure as compared with a conventional HM [54]. Because the interfacial coupling in a TI-FM structure is mainly associated with the TSS on the TI side, the relevant resistivity should be that of the bottom surface states. From conventional transport measurements, the measured resistivity ρ would be a convolution of the resistivities from the bulk and the top and bottom surfaces and hence is higher than the effective resistivity of each surface. Since the surface layer of Bi_2Se_3 hosting the topological states has a thickness of ~1 nm [55], which accounts for 5% of the entire thickness of the TI layer in our samples, the resistivity ρ measured from bulk transport should be significantly larger than the effective resistivity of the surface states. Considering this, a positive value of $1.4 \times 10^{14}\ \Omega^{-1}\ \mathrm{m}^{-2}$ is obtained when $\lambda_S = 1.6\,\mathrm{nm}$ [20]. However, the overestimated ρ alone still cannot fully explain the unexpected negative sign of $G_{\uparrow\downarrow}$ when using $\lambda_S = 6.2\,\mathrm{nm}$ [18] to calculate the value. Although a theoretical explanation of this discrepancy has not been established, it was suggested that the spin relaxation effect (e.g., spin memory loss) at the interface should also be considered to avoid an overestimated second term on the right side of Eq. (4) [21].

The resonantly excited spin current in Bi_2Se_3 via spin pumping generates an emf across the surface of the TI due to SML of the TSS. As shown in Fig. 2(e), we electrically detect this voltage response at resonance in a direction perpendicular to the applied external field. Here, we simultaneously measure the FMR and emf response caused using a small AC field on top of a DC bias field to enable lock-in detection for both. A representative plot of the emf voltage as a function of field at $f = 3\,\mathrm{GHz}$ is shown in Fig. 2(f) (blue curve). This signal bears many common features as the measured ISHE in HM-FM bilayer structures [53,56], namely, the appearance of a peak at the resonance field of the bilayer sample demonstrates the transfer of spin angular momentum across the interface between YIG and Bi_2Se_3.

The transfer of spin angular momentum across the interface can also affect the magneto-electronic transport properties of the bilayer structure. The scattering of the spin-polarized electrons generated on the Bi_2Se_3 surface would strongly depend on their relative orientation with the magnetization **M** of YIG, leading to an ADMR effect, which is analogous to the SHMR effect in HM-FM bilayer structures. Because HMs such as Pt, Pd, and Au show negligible angular dependence of MR, the measured ADMR in a HM-FM bilayer structure is a combination of SHMR and AMR, with the latter induced by the magnetic proximity effect [34] when the FM is an insulator such as YIG.

The measurement geometry is shown in Figs. 3(a)–3(c), where we define the direction of the current to be along x, the in-plane perpendicular direction as y, and the direction normal to the sample plane as z. As such, the AMR is a function of the component of **M** along the x direction, and SHMR is a function of the component of **M** along the y direction [9,53]:

$$\rho = \rho_0 + \Delta\rho_{\mathrm{AMR}} m_x^2, \tag{5}$$

$$\rho = \rho_0 + \Delta\rho_{\mathrm{SHMR}} m_y^2, \tag{6}$$

where $m_x = (\mathbf{M} \cdot \boldsymbol{x}/|\mathbf{M}|)$, $m_y = (\mathbf{M} \cdot \boldsymbol{y}/|\mathbf{M}|)$, ρ is the longitudinal resistivity, and ρ_0 is the zero-field longitudinal resistivity. Hence, by rotating the magnetization in the x-z plane [i.e., $m_y = 0$, Fig. 3(a)], AMR can be determined, and similarly, by rotating the magnetization in the y-z plane [i.e., $m_x = 0$, Fig. 3(b)], SHMR can be determined [9]. However, since Bi_2Se_3 is a layered material showing strong out-of-plane anisotropy in MR [57,58], its intrinsic AMR must also be considered in ADMR measurements.

The Bi_2Se_3 reference and Bi_2Se_3 film grown on YIG used in this paper are both degenerately doped, as evident from the metallic behavior of the temperature dependence of their longitudinal resistances, with similar resistance-change ratios (Fig. S2 in the Supplemental Material [46]). In addition, the Hall resistance R_{xy} of Bi_2Se_3-YIG-2 shows the expected sinusoidal dependence with field rotating in the x-z or y-z plane (Fig. S3(a) in the Supplemental Material [46]) and is linear with an out-of-plane magnetic field (Fig. S3(b) in the Supplemental Material [46]), confirming that anomalous Hall effect (AHE) is not present.

The ADMR of two Bi_2Se_3-YIG bilayer samples (Bi_2Se_3-YIG-1,2) and a Bi_2Se_3 reference sample (Bi_2Se_3-1) when the magnetic fields are rotated in the x-z plane (χ rotation), y-z plane (φ rotation), and x-y plane (ω rotation) are shown in Figs. 3(d)–3(f). Note that the applied fields (0.5 and 0.8 T) are well above the effective anisotropy field $\mu_0 M_{\mathrm{eff}}$ [$\approx 0.30\,\mathrm{T}$ as shown in Fig. 2(c)] or the saturation-magnetization field $\mu_0 M_S$ ($\approx 0.18\,\mathrm{T}$) of the YIG layer, hence the magnetization direction of YIG should orient along the field direction. As such, according to Eqs. (5) and (6), the ADMR is expected to follow $\cos^2\chi$ and $\cos^2\varphi$ for χ and φ rotations, respectively [9]. However, as shown in Figs. 3(d) and 3(e), the measured out-of-plane ADMR clearly deviates from this dependence (dashed curves), suggesting that neither SHMR nor AMR alone can explain these observations. Moreover, in an earlier study, Chiba *et al.* [59] predicted that the interfacial coupling between a TI and a FM insulator can simultaneously lead to AMR and non-sine-dependent transverse resistance/conductivity for out-of-plane rotations. However, as shown in Fig. S3(a) in the

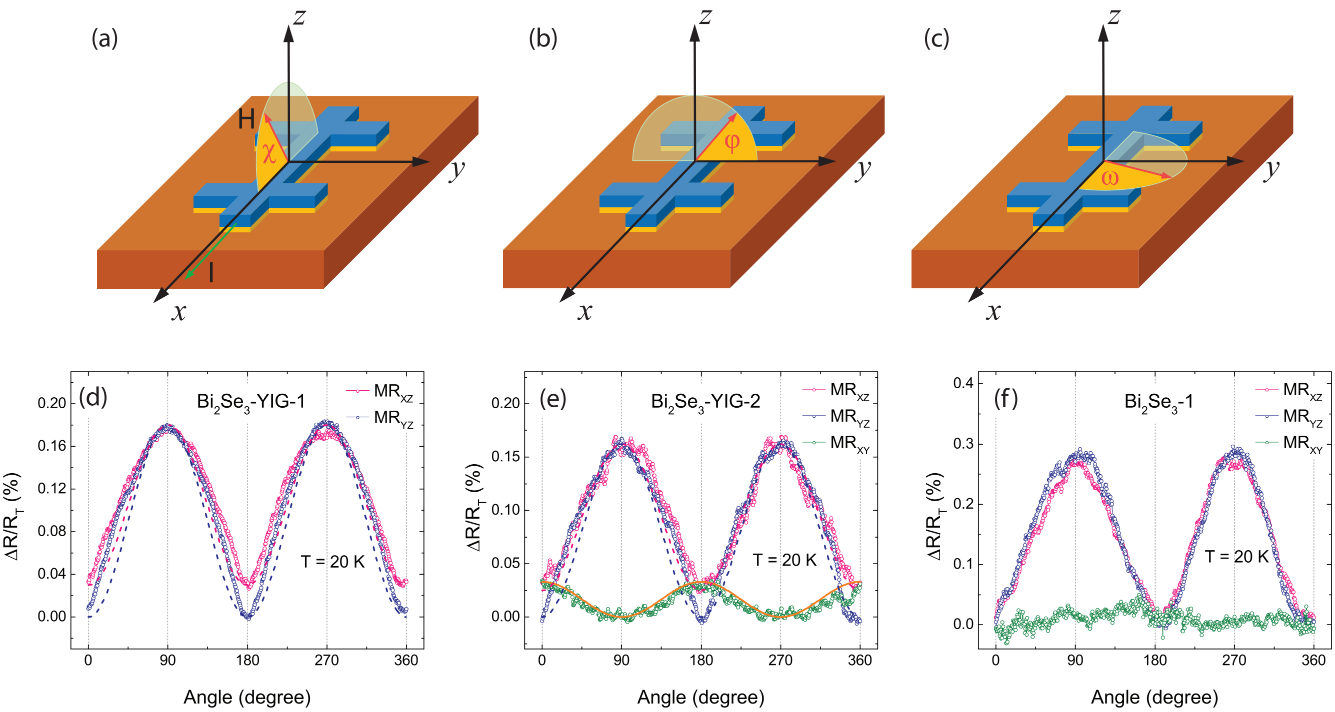

FIG. 3. (a)–(c) Schematics for χ, φ, and ω rotations, respectively. (d)–(f) Angle-dependent magnetoresistance (ADMR) of Bi_2Se_3-YIG-1, Bi_2Se_3-YIG-2, and Bi_2Se_3-1 in magnetic fields of 0.5, 0.8, and 0.8 T, respectively. In (d) and (e), each dashed curve is a fit for the corresponding out-of-plane ADMR data (χ or φ rotation) based on Eqs. (5) and (6), and in (e), the in-plane ADMR (ω rotation) follows cosine-squared dependence indicated by an orange curve.

Supplemental Material [46], we found that the transverse resistance measured for an out-of-plane rotation of a Bi_2Se_3-YIG sample in a magnetic field of 0.8 T can be well described by a sine function, indicating that the theory proposed by Chiba *et al.* [59] cannot explain the observed out-of-plane ADMR in the bilayer sample.

On the other hand, we note that the ADMR of all three samples share a few similarities. Specifically, the resistances of the samples all show a maximum value when the magnetic field is along the z direction [90° and 270° for x-z and y-z rotations in Figs. 3(d)–3(f)] and decrease significantly when the field rotates away, resulting in strongly V-shaped dependence near the in-plane directions. Such V-shaped angular dependence is a signature of the out-of-plane AMR of layered materials [60,61], suggesting that the measured ADMR of the Bi_2Se_3-YIG bilayer structure includes a substantial contribution from the intrinsic MR of Bi_2Se_3.

When the magnetic field rotates in the sample plane (ω rotation), the resistance of Bi_2Se_3-1 is nearly angular independent [Fig. 3(f)], while the resistance of Bi_2Se_3-YIG-2 follows cosine-squared dependence [Fig. 3(e)], which is consistent with in-plane anisotropy of SHMR or AMR. An in-plane MR ratio, defined by $(R^x\text{-}R^y)/R^y$, of $\sim$0.04% can be extracted from these results obtained on the two Bi_2Se_3-YIG samples. The emergence of this additional variation/angle dependence in the in-plane MR in the presence of the YIG layer clearly indicates influence from the interfacial coupling between the two layers. As mentioned earlier, exceptionally large out-of-plane transport anisotropy has been observed in several TI-FM transport studies [24–27], but how to extract the portion of the ADMR that is associated with the interfacial interaction and further determine the SCC efficiency in the TI has not been addressed previously. In this paper, we indicate that subtraction of the intrinsic ADMR of the layered TI material is an essential step to quantitatively determine the SCC efficiency based on ADMR measurements.

The temperature dependence of the ADMR of a Bi_2Se_3-YIG bilayer sample with a 0.8 T field rotated in the x-z and y-z planes are shown in Figs. S4(a) and S4(b) in the Supplemental Material [46], respectively. As temperature increases, the MR decreases for both rotations at temperatures $<$100 K and then becomes nearly temperature independent. In contrast, the MR of the Bi_2Se_3 reference sample decreases steadily over the entire temperature range for both rotations (Figs. S4(c) and S4(d) in the Supplemental Material [46]). These observations are summarized in Fig. 4(a), where the resistance difference ΔR is defined as $\Delta R^{z\text{-}x} = R^z - R^x$ for χ rotations, and $\Delta R^{z\text{-}y} = R^z - R^y$ for φ rotations. For the Bi_2Se_3-YIG bilayer sample, $\Delta R^{z\text{-}y}$ and $\Delta R^{z\text{-}x}$ show a clear difference at temperatures $<$100 K and are nearly the same $>$100 K. In other words, the in-plane variation in the longitudinal resistance of Bi_2Se_3-YIG-2 emerges when temperature is reduced to $\sim$100 K, i.e., a temperature consistent with the characteristic temperature found for the TSS becoming dominant in earlier spin detection measurements [37]. In contrast, for the Bi_2Se_3 reference sample, $\Delta R^{z\text{-}y}$ and $\Delta R^{z\text{-}x}$ nearly coincide with each other over the entire temperature range, indicating a lack of in-plane anisotropy. Therefore, the temperature dependence of the ADMR suggests that the nontrivial topological nature of Bi_2Se_3 is the origin of the observed in-plane ADMR in the Bi_2Se_3-YIG bilayer structure.

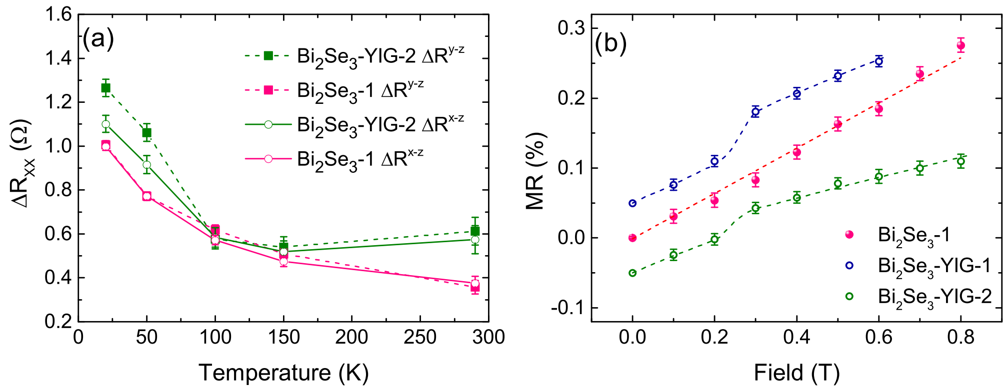

FIG. 4. (a) Measured resistance difference ΔR as a function of temperature for Bi_2Se_3-YIG-2 and Bi_2Se_3-1. (b) Field dependence of $\Delta R^{z\text{-}y}/R^{y}$ for Bi_2Se_3-YIG-1, Bi_2Se_3-YIG-2, and Bi_2Se_3-1. Note: Data for Bi_2Se_3-YIG-1 and Bi_2Se_3-YIG-2 are shifted vertically by 0.05 and −0.05%, respectively, for clarity.

The magnetic field dependence of the MR ratio for φ rotations (i.e., $\Delta R^{z\text{-}y}/R^{y}$) of all three samples at 20 K are shown in Fig. 4(b) (the ADMR curves at different magnetic fields are shown in Fig. S5 in the Supplemental Material [46]). Interestingly, while the MR ratio increases linearly with field for the Bi_2Se_3 sample, there is a clear increase in slope between 0.2 to 0.3 T for the two Bi_2Se_3-YIG samples. As discussed above, our FMR measurements indicate that the effective anisotropy field $\mu_0 M_{\text{eff}}$ also lies within this range, suggesting that this enhancement in MR ratio is related to when the magnetization of YIG begins to strictly follow the direction of the applied field. These results suggest that interfacial coupling between YIG and the Bi_2Se_3 indeed contributes to the MR ratio of the heterostructure.

The ADMR of the Bi_2Se_3-YIG bilayer structure observed in ω rotation may include contributions from the following three possible mechanisms: first, two-dimensional (2D) SCC associated with the SML of the TSS of Bi_2Se_3; second, 3D SCC associated with the strong SOC of bulk Bi_2Se_3 (i.e., conventional SHMR); and third, anisotropic spin scattering associated with proximity-induced FM in Bi_2Se_3 (i.e., AMR) [34]. Here, the first mechanism can be regarded as a quantum limit of the second mechanism, and the corresponding ADMR also follows Eq. (6). For simplicity, in the following, we refer to the MR due to the first two mechanisms as SCCMR.

Like the SHMR and AMR in HM-FM structures, the SCCMR and AMR in the Bi_2Se_3-YIG bilayer structure only differ when the applied field rotates away from the sample plane. However, the pronounced intrinsic out-of-plane MR of Bi_2Se_3 in the measured ADMR of the bilayer structure makes it challenging to independently determine the SCCMR and AMR. In an earlier work, a low-field anomaly in two-point transport measurements of a Bi_2Se_3 flake exfoliated onto a YIG substrate had been interpreted as a signature of proximity-induced magnetism [62]. However, this anomaly is only present $<\sim$4 K, and there is no angular dependence of the MR at high fields [62]. Hence, even though proximity-induced magnetism can occur in Bi_2Se_3-YIG bilayers at low temperatures, it does not explain our ADMR results, particularly at much higher temperatures. Moreover, since magnetic proximity-induced AMR should always accompany AHE [34,63,64], the absence of AHE in our Hall resistance measurements would also rule out the contribution of AMR in the longitudinal resistance measurements.

To further determine the contributions to the SCCMR from 2D SCC and conventional SHMR, the temperature dependence of the ADMR discussed above [Fig. 4(a)] provides important information. Specifically, the fact that the in-plane anisotropy of the MR emerging at a temperature where the TSS is likely to dominate transport [37] would suggest that the topological nature of Bi_2Se_3 plays a significant role in the in-plane AMR. In addition, because the conventional SHMR is predominately determined by the spin Hall angle which typically shows weak temperature dependence, the SHMR ratio is not expected to vary significantly as a function of temperature [64–66]. Hence, the enhanced in-plane anisotropy $<$100 K [Fig. 4(a)] and the in-plane MR ratio of $\sim$0.04% at 20 K can be attributed to the 2D SCC associated with the SML of the TSS.

It is known that, for an HM-FM bilayer structure, the spin Hall angle of the HM can be calculated from the ADMR (i.e., SHMR) ratio based on the following equation [53]:

$$\left|\frac{\Delta R}{R_0}\right| = \frac{\theta_{\text{SH}}^2 \frac{2\lambda_S^2\rho}{t_{\text{HM}}} G_{\uparrow\downarrow} \tanh^2\left(\frac{t_{\text{HM}}}{2\lambda_S}\right)}{1 + 2\lambda_S\rho\, G_{\uparrow\downarrow}\, \coth\left(\frac{t_{\text{HM}}}{\lambda_S}\right)}, \tag{7}$$

where θ_{SH} is the spin Hall angle, λ_S the vertical spin diffusion length, and t_{HM} and ρ the thickness and bulk resistivity, respectively, of the HM. It should be noted that Eq. (7) was derived based on a 3D charge-to-spin interconversion picture, and its application to 2D charge-to-spin interconversion can be problematic. In several earlier FMR-driven spin-pumping studies [20,23,67–70], a parameter λ_{IEE} with the dimension of length has been used to describe the SCC efficiency in TIs, and $\lambda_{\text{IEE}} = j_C^{2D}/j_S^{3D} = v_F \cdot \tau$, where j_C^{2D} is the surface charge current density, j_S^{3D} the vertical spin current density, v_F the Fermi velocity of the TSS, and τ the spin scattering time associated with the 2D SCC. On the other hand, the term *effective spin Hall angle* (or *SOT efficiency*) has been widely adopted to describe the conversion efficiency in TIs. Though not a perfect analogy and not specifically developed for a 2D system, it does provide a quantitative measure for direct comparison to charge-to-spin conversion efficiencies in HMs. Specifically, since the 2D spin-to-charge interconversion takes place within a certain depth at the interface, the parameter λ_{IEE} can be divided by this finite thickness to yield a dimensionless value for direct comparison with the spin Hall angle of HMs [21,23,71].

Here, we similarly consider the effective thickness of TSS by regarding the TI as a three-layer system: a bottom TSS layer interfaced with YIG, a bulk layer, and a top TSS layer. Based on Eq. (7) and using the resistivity ($2.0 \times 10^{-6}\,\Omega\,\mathrm{m}$) and the thickness (1 nm) of the TSS layer, $G_{\uparrow\downarrow} = G_{\mathrm{eff}} \approx 5.0 \times 10^{13}\Omega^{-1}\,\mathrm{m}^{-2}$, and the vertical spin diffusion lengths 1.6 nm [20] and 6.2 nm [18] reported in literature, we determine a value of 0.1–0.4 for the effective spin Hall angle of Bi_2Se_3. It should be noted that the assumption of a completely insulating bulk may be simplistic, especially when the Bi_2Se_3 film is degenerately doped. However, because the spin diffusion length is short and the interfacial coupling is mainly established between the bottom TSS layer and YIG, bulk conduction in the Bi_2Se_3 film is expected to only result in a small correction term to the estimate. On the other hand, if the MR ratio in the *y-z* plane [e.g., 0.18% according to Fig. 3(d)] is mistakenly considered as fully associated with the 2D spin-to-charge interconversion in the bilayer structure, it will result in an overestimate of the effective spin Hall angle by a factor of ∼5. For comparison, we further list our experimental method and estimated effective spin Hall angle in Table I. In contrast to the methods used in previous studies, our approach to extract the spin-to-charge efficiency in the TI is based on a combined study of FMR, IREE, and ADMR measurements.

Finally, we discuss possible contributions from SSE [72–74] to the observed ADMR. In the Bi_2Se_3-YIG bilayer structure, passing a charge current through the Bi_2Se_3 layer can generate a substantial temperature gradient in the direction perpendicular to the sample plane due to Joule heating. This temperature gradient can further induce a vertical spin current in Bi_2Se_3 via the SSE [73,74], and through SCC, the spin current can in turn affect the longitudinal transport, leading to ADMR [9]. According to Joule's law, the spin current should be proportional to the square of the charge current, and thus, the MR ratio should linearly depend on the charge current. In our measurements, the MR ratio is found to be insensitive to the magnitude of the current (Fig. S6 in the Supplemental Material [46]), thus ruling out contribution from SSE to the measured ADMR.

IV. CONCLUSIONS

In this paper, we systematically investigate the spin-to-charge interconversion in a Bi_2Se_3-YIG bilayer structure. FMR measurements reveal an enhanced damping in the YIG due to spin pumping into Bi_2Se_3 and yield a spin-mixing conductance $G_{\mathrm{eff}} \approx 5.0 \times 10^{13}\Omega^{-1}\,\mathrm{m}^{-2}$. The robust interfacial coupling is also confirmed by the detection of an emf generated in Bi_2Se_3 at FMR of the bilayer structure. Systematic ADMR measurements in all three planes of the Bi_2Se_3-YIG bilayer structure and a Bi_2Se_3 reference film indicate that, in direct contrast to the negligible intrinsic ADMR of HMs, the intrinsic ADMR of Bi_2Se_3 itself must be considered to extract the MR associated with the charge-to-spin interconversion. Moreover, ruling out contribution from proximity-induced magnetism in the Bi_2Se_3 due to absence of AHE, we determine that the MR ratio associated with the interfacial interaction between the YIG and the Bi_2Se_3 is ∼0.04% at 20 K. Based on these results, we further estimate an effective spin Hall angle of ∼0.1–0.4 for Bi_2Se_3.

ACKNOWLEDGMENTS

The authors gratefully acknowledge financial support from the Applied Research for the Advancement of ST Priorities program on Topologically Enabled Devices sponsored by the Office of the Under Secretary of Defense (Research & Engineering).

[1] A. D. Kent and D. C. Worledge, A new spin on magnetic memories, Nat. Nanotech. **10**, 187 (2015).

[2] L. Berger, Emission of spin waves by a magnetic multilayer traversed by a current, Phys. Rev. B **54**, 9353 (1996).

[3] J. C. Slonczewski, Current-driven excitation of magnetic multilayers, J. Magn. Magn. Mater. **159**, L1 (1996).

[4] J. E. Hirsch, Spin Hall Effect, Phys. Rev. Lett. **83**, 1834 (1999).

[5] K. Uchida, S. Takahashi, K. Harii, J. Ieda, W. Koshibae, K. Ando, K. Maekawa, and E. Saitoh, Observation of the spin Seebeck effect, Nature (London) **455**, 778 (2008).

[6] A. Manchon, J. Železný, I. M. Miron, T. Jungwirth, J. Sinova, A. Thiaville, K. Garello, and P. Gambardella, Current-induced spin-orbit torques in ferromagnetic and antiferromagnetic systems, Rev. Mod. Phys. **91**, 035004 (2019).

[7] K. Garello, F. Yasin, S. Couet, L. Souriau, J. Swerts, S. Rao, S. van Beek, W. Kim, E. Liu, S. Kundu *et al.*, SOT-MRAM 300MM integration for low power and ultrafast embedded memories, *2018 IEEE Symposium on VLSI Circuits* (IEEE, Honolulu, 2018), pp. 81–82.

[8] M. I. Dyakonov and V. I. Perel, Current-induced spin orientation of electrons in semiconductors, Phys. Lett. A **35**, 459 (1971).

[9] H. Nakayama, M. Althammer, Y.-T. Chen, K. Uchida, Y. Kajiwara, D. Kikuchi, T. Ohtani, S. Geprägs, M. Opel, S. Takahashi *et al.*, Spin Hall Magnetoresistance Induced by a Nonequilibrium Proximity Effect, Phys. Rev. Lett. **110**, 206601 (2013).

[10] S. Cho, S.-H. C. Baek, K.-D. Lee, Y.-H. Jo, and B.-G. Park, Large spin Hall magnetoresistance and its correlation to the spin-orbit torque in W/CoFeB/MgO structures, Sci. Rep. **5**, 14668 (2015).

[11] A. R. Mellnik, J. S. Lee, A. Richardella, J. L. Grab, P. J. Mintun, M. H. Fischer, A. Vaezi, A. Manchon, E.-A. Kim, N. Samarth, and D. C. Ralph, Spin-transfer torque generated by a topological insulator, Nature (London) **511**, 449 (2014).

[12] L. Liu, A. Richardella, I. Garate, Y. Zhu, N. Samarth, and C.-T. Chen, Spin-polarized tunneling study of spin-momentum locking in topological insulators, Phys. Rev. B **91**, 235437 (2015).

[13] N. H. D. Khang, Y. Ueda, and P. N. Hai, A conductive topological insulator with large spin Hall effect for ultralow power spin-orbit torque switching, Nat. Mater. **17**, 808 (2018).

[14] H. L. Wang, J. Kally, C. Şahin, T. Liu, W. Yanez, E. J. Kamp, A. Richardella, M. Z. Wu, M. E. Flatté, and N. Samarth, Fermi level dependent spin pumping from a magnetic insulator into a topological insulator, Phys. Rev. Res. **1**, 012014(R) (2019).

[15] Y. B. Fan, P. Upadhyaya, X. F. Kou, M. R. Lang, S. Takei, Z. X. Wang, J. S. Tang, L. He, L.-T. Chang, M. Montazeri *et al.*, Magnetization switching through giant spin-orbit torque in a magnetically doped topological insulator heterostructure, Nat. Mater. **13**, 699 (2014).

[16] K. Yasuda, A. Tsukazaki, R. Yoshimi, K. Kondou, K. S. Takahashi, Y. Otani, M. Kawasaki, and Y. Tokura, Current-Nonlinear Hall Effect and Spin-Orbit Torque Magnetization Switching in a Magnetic Topological Insulator, Phys. Rev. Lett. **119**, 137204 (2017).

[17] P. N. Petrov, M. D. Davydova, P. N. Skirdkov, K. A. Zvezdin, J. G. Lin, and J. C. A. Huang, Inverse spin Hall effect in heterostructures "nanostructured ferromagnet/topological insulator", EPJ Web Conf. **185**, 01005 (2018).

[18] P. Deorani, J. S. Son, K. Banerjee, N. Koirala, M. Brahlek, S. S. Oh, and H. S. Yang, Observation of inverse spin hall effect in bismuth selenide, Phys. Rev. B **90**, 094403 (2014).

[19] M. Jamali, J. S. Lee, J. S. Jeong, F. Mahfouzi, Y. Lv, Z. Y. Zhao, B. K. Nikolić, K. A. Mkhoyan, N. Samarth, and J.-P. Wang, Giant spin pumping and inverse spin Hall effect in the presence of surface and bulk spin-orbit coupling of topological insulator Bi_2Se_3, Nano Lett. **15**, 7126 (2015).

[20] H. L. Wang, J. Kally, J. S. Lee, T. Liu, H. C. Chang, D. R. Hickey, K. A. Mkhoyan, M. Z. Wu, A. Richardella, and N. Samarth, Surface-State-Dominated Spin-Charge Current Conversion in Topological-Insulator-Ferromagnetic-Insulator Heterostructures, Phys. Rev. Lett. **117**, 076601 (2016).

[21] D. P. Zhu, Y. Wang, S. Y. Shi, K.-L. Teo, Y. H. Wu, and H. S. Yang, Highly efficient charge-to-spin conversion from *in situ* Bi_2Se_3/Fe heterostructures, Appl. Phys. Lett. **118**, 062403 (2021).

[22] Y. Wang, P. Deorani, K. Banerjee, N. Koirala, M. Brahlek, S. S. Oh, and H. S. Yang, Topological Surface States Originated Spin-Orbit Torques in Bi_2Se_3, Phys. Rev. Lett. **114**, 257202 (2015).

[23] K. Kondou, R. Yoshimi, A. Tsukazaki, Y. Fukuma, J. Matsuno, K. S. Takahashi, M. Kawasaki, Y. Tokura, and Y. Otani, Fermi-level-dependent charge-to-spin current conversion by Dirac surface states of topological insulators, Nat. Phys. **12**, 1027 (2016).

[24] K. Yasuda, A. Tsukazaki, R. Yoshimi, K. S. Takahashi, M. Kawasakio, and Y. Tokura, Large Unidirectional Magnetoresistance in a Magnetic Topological Insulator, Phys. Rev. Lett. **117**, 127202 (2016).

[25] N. H. D. Khang and P. N. Hai, Giant unidirectional spin Hall magnetoresistance in topological insulator-ferromagnetic semiconductor heterostructures, J. Appl. Phys. **126**, 233903 (2019).

[26] Y. Lv, J. Kally, D. L. Zhang, J. S. Lee, M. Jamali, N. Samarth, and J.-P. Wang, Unidirectional spin-Hall and Rashba-Edelstein magnetoresistance in topological insulator ferromagnet layer heterostructures, Nat. Commun. **9**, 111 (2018).

[27] Y. Lv, J. Kally, T. Liu, P. Qurarterman, T. Pillsbury, B. J. Kirby, A. J. Grutter, P. Sahu, J. A. Borchers, M. Z. Wu *et al.*, Large unidirectional spin hall and rashba-edelstein magnetoresistance in topological insulator/magnetic insulator heterostructures, Appl. Phys. Rev. **9**, 011406 (2022).

[28] T. McGuire and R. Potter, Anisotropic magnetoresistance in ferromagnetic 3*d* alloys, IEEE Trans. Magn. **11**, 1018 (1975).

[29] C. Kittel, Ferromagnetic resonance, J. Phys. Radium **12**, 291 (1951).

[30] T. Taniguchi and H. Imamura, Enhancement of the Gilbert damping constant due to spin pumping in noncollinear ferromagnet/nonmagnet/ferromagnet trilayer systems, Phys. Rev. B **76**, 092402 (2007).

[31] Y. Shiomi, K. Nomura, Y. Kajiwara, K. Eto, M. Novak, K. Segawa, Y. Ando, and E. Saitoh, Spin-Electricity Conversion Induced by Spin Injection into Topological Insulators, Phys. Rev. Lett. **113**, 196601 (2014).

[32] J. H. Han, A. Richardella, S. A. Siddiqui, J. Finley, N. Samarth, and L. Q. Liu, Room-Temperature Spin-Orbit Torque Switching Induced by a Topological Insulator, Phys. Rev. Lett. **119**, 077702 (2017).

[33] J. Zhang, J. P. Velev, X. Q. Dang, and E. Y. Tsymbal, Band structure and spin texture of Bi_2Se_3 3*d* ferromagnetic metal interface, Phys. Rev. B **94**, 014435 (2016).

[34] S. Y. Huang, X. Fan, D. Qu, Y. P. Chen, W. G. Wang, J. Wu, T. Y. Chen, J. Q. Xiao, and C. L. Chien, Transport Magnetic Proximity Effects in Platinum, Phys. Rev. Lett. **109**, 107204 (2012).

[35] M. A. W. Schoen, D. Thonig, M. L. Schneider, T. J. Silva, H. T. Nembach, O. Eriksson, O. Karis, and J. M. Shaw, Ultra-low magnetic damping of a metallic ferromagnet, Nat. Phys. **12**, 839 (2016).

[36] B. M. Howe, S. Emori, H.-M. Jeon, T. M. Oxholm, J. G. Jones, K. Mahalingam, Y. Zhuang, N. X. Sun, and G. J. Brown, Pseudomorphic yttrium iron garnet thin films with low damping and inhomogeneous linewidth broadening, IEEE Magnet. Lett. **6**, 3500504 (2015).

[37] C. H. Li, O. M. J. van 't Erve, J. T. Robinson, Y. Liu, L. Li, and B. T. Jonker, Electrical detection of charge-current-induced spin polarization due to spin-momentum locking in Bi_2Se_3, Nat. Nanotech. **9**, 218 (2014).

[38] H. D. Li, Z. Y. Wang, X. Kan, X. Guo, H. T. He, Z. Wang, J. N. Wang, T. L. Wong, N. Wang, and M. H. Xie, The van der Waals epitaxy of Bi_2Se_3 on the vicinal Si(111) surface: an approach for preparing high-quality thin films of a topological insulator, New J. Phys. **12**, 103038 (2011).

[39] L. He, F. X. Xiu, Y. Wang, A. V. Fedorov, G. Huang, X. F. Kou, M. R. Lang, W. P. Beyermann, J. Zou, and K. L. Wang, Epitaxial growth of Bi2Se3 topological insulator thin films on Si (111), J. Appl. Phys. **109**, 103702 (2011).

[40] S. Xu, Y. Han, X. L. Chen, Z. F. Wu, L. Wang, T. Y. Han, W. G. Ye, H. H. Lu, G. Long, Y. Y. Wu *et al.*, van der Waals epitaxial growth of atomically thin Bi_2Se_3 and thickness-dependent topological phase transition, Nano Lett. **15**, 2645 (2015).

[41] D. Bahadur, Current trends in applications of magnetic ceramic materials, Bull. Mater. Sci. **15**, 431 (1992).

[42] Y. Kajiwara, K. Harii, S. Takahashi, J. Ohe, K. Uchida, M. Mizuguchi, H. Umezawa, H. Kawai, K. Ando, K. Takanashi *et al.*, Transmission of electrical signals by spin-wave interconversion in a magnetic insulator, Nature (London) **464**, 262 (2010).

[43] C. Hauser, T. Richter, N. Homonnay, C. Eisenschmidt, M. Qaid, H. Deniz, D. Hesse, M. Sawicki, S. G. Ebbinghaus, and G.

Schmidt, Yttrium iron garnet thin films with very low damping obtained by recrystallization of amorphous material, Sci. Rep. **6**, 20827 (2016).

[44] C. Tang, Q. Song, C.-Z. Chang, Y. D. Xu, Y. Ohnuma, M. Matsuo, Y. W. Liu, W. Yuan, Y. Y. Yao, J. S. Moodera *et al.*, Dirac surface state-modulated spin dynamics in a ferrimagnetic insulator at room temperature, Sci. Adv. **4**, eaas8660 (2018).

[45] Y. Tserkovnyak, A. Brataas, G. E. W. Bauer, and B. I. Halperin, Nonlocal magnetization dynamics in ferromagnetic heterostructures, Rev. Mod. Phys. **77**, 1375 (2005).

[46] See Supplemental Material at http://link.aps.org/supplemental/10.1103/PhysRevMaterials.6.074203 for additional data and detailed analysis.

[47] C. T. Boone, H. T. Nembach, J. M. Shaw, and T. J. Silva, Spin transport parameters in metallic multilayers determined by ferromagnetic resonance measurements of spin pumping, J. Appl. Phys. **113**, 153906 (2013).

[48] Y. T. Fanchiang, K. H. M. Chen, C. C. Tseng, C. C. Chen, C. K. Cheng, S. R. Yang, C. N. Wu, S. F. Lee, M. Hong, and J. Kwo, Strongly exchange-coupled and surface-state-modulated magnetization dynamics in Bi_2Se_3/yttrium iron garnet heterostructures, Nat. Commun. **9**, 223 (2018).

[49] B. Heinrich, C. Burrowes, E. Montoya, B. Kardasz, E. Girt, Y.-Y. Song, Y. Y. Sun, and M. Z. Wu, Spin Pumping at the Magnetic Insulator (YIG)/Normal Metal (Au) Interfaces, Phys. Rev. Lett. **107**, 066604 (2011).

[50] O. Mosendz, V. Vlaminck, J. E. Pearson, F. Y. Fradin, G. E. W. Bauer, S. D. Bader, and A. Hoffmann, Detection and quantification of inverse spin Hall effect from spin pumping in permalloy/normal metal bilayers, Phys. Rev. B **82**, 214403 (2010).

[51] H. L. Wang, C. H. Du, Y. Pu, R. Adur, P. C. Hammel, and F. Y. Yang, Scaling of Spin Hall Angle in 3*d*, 4*d*, 5*d* Metals from Y_3Fe_5O/metal Spin Pumping, Phys. Rev. Lett. **112**, 197201 (2014).

[52] G. Consolo, G. Finocchio, G. Siracusano, S. Bonetti, A. Eklund, J. Åkerman, and B. Azzerboni, Non-stationary excitation of two localized spin-wave modes in a nano-contact spin torque oscillator, J. Appl. Phys. **114**, 153906 (2013).

[53] M. T. Gray, S. Emori, B. A. Gray, H. Jeon, O. M. J. van 't Erve, B. T. Jonker, S. Kim, M. Suzuki, T. Ono, B. M. Howe *et al.*, Spin-Current Generation in Low-Damping $Ni_{0.65}Zn_{0.35}Al_{0.8}Fe_{1.2}O_4$ Spinel Ferrite, Phys. Rev. Applied **9**, 064039 (2018).

[54] J.-C. Rojas-Sánchez and A. Fert, Compared Efficiencies of Conversions between Charge and Spin Current by Spin-Orbit Interactions in Two- and Three-Dimensional Systems, Phys. Rev. Applied **11**, 054049 (2019).

[55] B. H. Yan, D. L. Zhang, and C. Felser, Topological surface states of Bi_2Se_3 coexisting with Se vacancies, Phys. Status Solidi RRL **7**, 148 (2013).

[56] J.-C. Rojas-Sánchez, N. Reyren, P. Laczkowski, W. Savero, J.-P. Attané, C. Deranlot, M. Jamet, J.-M. George, L. Vila, and H. Jaffrès, Spin Pumping and Inverse Spin Hall Effect in Platinum: The Essential Role of Spin-Memory Loss at Metallic Interfaces, Phys. Rev. Lett. **112**, 106602 (2014).

[57] H. T. He, B. K. Li, H. C. Liu, X. Guo, Z. Y. Wang, M. H. Xie, and J. N. Wang, High-field linear magneto-resistance in topological insulator Bi_2Se_3 thin films, Appl. Phys. Lett. **100**, 032105 (2012).

[58] H. Pan, S. S.-L. Zhang, D. P. Zhu, Y. Liu, Y. Wang, J. W. Yu, G. Vignale, and H. S. Yang, Bilinear magnetoelectric resistance as a probe of three-dimensional spin texture in topological surface states, Nat. Phys. **14**, 495 (2018).

[59] T. Chiba, S. Takahashi, and G. E. W. Bauer, Magnetic-proximity-induced magnetoresistance on topological insulators, Phys. Rev. B **95**, 094428 (2017).

[60] H. Tang, D. Liang, R. L. J. Qiu, and X. P. A. Gao, Two-dimensional transport-induced linear magneto-resistance in topological insulator Bi_2Se_3 nanoribbons, ACS Nano **5**, 7510 (2011).

[61] Y. F. Zhao, C.-Z. Chang, Y. Jiang, A. DaSilva, Y. Sun, H. C. Wang, Y. Xing, Y. Wang, K. He, X. C. Ma *et al.*, Demonstration of surface transport in a hybrid Bi_2Se_3/Bi_2Te_3 heterostructure, Sci. Rep. **3**, 3060 (2013).

[62] J. Sklenar, Y. J. Zhang, M. B. Jungfleisch, Y. S. Kim, Y. R. Xiao, G. J. MacDougall, M. J. Gilbert, A. Hoffmann, P. Schiffer, and N. Mason, Proximity-induced anisotropic magnetoresistance in magnetized topological insulators, Appl. Phys. Lett. **118**, 232402 (2021).

[63] W. Amamou, I. V. Pinchuk, A. H. Trout, R. E. A. Williams, N. Antolin, A. Goad, D. J. O'Hara, A. S. Ahmed, W. Windl, D. W. McComb *et al.*, Magnetic proximity effect in Pt/$CoFe_2O_4$ bilayers, Phys. Rev. Materials **2**, 011401(R) (2018).

[64] T. Shang, Q. F. Zhan, L. Ma, H. L. Yang, Z. H. Zuo, Y. L. Xie, H. H. Li, L. P. Liu, B. M. Wang, Y. H. Wu *et al.*, Pure spin-Hall magnetoresistance in Rh/$Y_3Fe_5O_{12}$ hybird, Sci. Rep. **5**, 17734 (2015).

[65] S. R. Marmion, M. Ali, M. McLaren, D. A. Williams, and B. J. Hickey, Temperature dependence of spin Hall magnetoresistance in thin YIG/Pt films, Phys. Rev. B **89**, 220404(R) (2014).

[66] T. Okuno, T. Taniguchi, S. H. Kim, S.-H. Baek, B.-G. Park, T. Moriyama, K.-J. Kim, and T. Ono, Temperature dependence of spin Hall magnetoresistance in W/CoFeB bilayer, Jpn. J. Appl. Phys. **55**, 080308 (2016).

[67] J.-C. Rojas-Sánchez, S. Oyarzún, Y. Fu, A. Marty, C. Vergnaud, S. Gambarelli, L. Vila, M. Jamet, Y. Ohtsubo, A. Taleb-Ibrahimi *et al.*, Spin to Charge Conversion at Room Temperature by Spin Pumping into a New Type of Topological Insulator: A-Sn Films, Phys. Rev. Lett. **116**, 096602 (2016).

[68] J. B. S. Mendes, O. Alves Santos, J. Holanda, R. P. Loreto, C. I. L. de Araujo, Cui-Zu Chang, J. S. Moodera, A. Azevedo, and S. M. Rezende, Dirac-surface-state-dominated spin to charge current conversion in the topological insulator $(Bi_{0.22}Sb_{0.78})_2Te_3$ films at room temperature, Phys. Rev. B **96**, 180415(R) (2017).

[69] H. R. He, L. X. Tai, D. Wu, H. Wu, A. Razavi, K. Wong, Y. X. Liu, and K. L. Wang, Enhancement of spin-to-charge conversion efficiency in topological insulators by interface engineering, APL Mater. **9**, 071104 (2021).

[70] K. Shen, G. Vignale, and R. Raimondi, Microscopic Theory of the Inverse Edelstein Effect, Phys. Rev. Lett. **112**, 096601 (2014).

[71] J.-C. Rojas-Sánchez, L. Vila, G. Desfonds, S. Gambarelli, J.-P. Attané, J. M. De Teresa, C. Magén, and A. Fert, Spin-to-charge conversion using Rashba coupling at the interface between non-magnetic materials, Nat. Commun. **4**, 2944 (2013).

[72] C. O. Avci, K. Garello, A. Ghosh, M. Gabureac, S. F. Alvarado, and P. Gambardella, Unidirectional spin Hall magnetoresis-

tance in ferromagnet/normal metal bilayers, Nat. Phys. **11**, 570 (2015).

[73] B. F. Miao, S. Y. Huang, D. Qu, and C. L. Chien, Inverse Spin Hall Effect in a Ferromagnetic Metal, Phys. Rev. Lett. **111**, 066602 (2013).

[74] W. X. Wang, S. H. Wang, L. K. Zou, J. W. Cai, Z. G. Sun, and J. R. Sun, Joule heating-induced coexisted spin Seebeck effect and spin Hall magnetoresistance in the platinum/Y_3Fe_5O structure, Appl. Phys. Lett. **105**, 182403 (2014).